J. F. Zhang
Key Laboratory of Thermo-Fluid Science and Engineering,
Ministry of Education,
School of Energy and Power Engineering,
Xi'an Jiaotong University,
Xi'an 710049, China

S. Wang
Key Laboratory of Thermo-Fluid Science and Engineering,
Ministry of Education,
School of Energy and Power Engineering,
Xi'an Jiaotong University,
Xi'an 710049, China

M. J. Zeng
Key Laboratory of Thermo-Fluid Science and Engineering,
Ministry of Education,
School of Energy and Power Engineering,
Xi'an Jiaotong University,
Xi'an 710049, China

Z. G. Qu[1]
Key Laboratory of Thermo-Fluid Science and Engineering,
Ministry of Education,
School of Energy and Power Engineering,
Xi'an Jiaotong University,
Xi'an 710049, China
e-mail: zgqu@mail.xjtu.edu.cn

Experimental and Numerical Investigation on Flow Characteristics of Large Cross-Sectional Ionic Wind Pump With Multiple Needles-to-Mesh Electrode

Ionic wind pumps have attracted considerable interest because of their low energy consumption, compact structures, flexible designs, and lack of moving parts. However, large cross-sectional ionic wind pumps have yet to be numerically analyzed and experimentally optimized. Accordingly, this study develops a large cross-sectional ionic wind pump with multiple needles-to-mesh electrode, as well as analyzes its flow characteristics using a proposed full three-dimensional simulation method validated with experimental data. To obtain a considerably high outlet average velocity, experimental studies and numerical methods are employed to optimize the pump's configuration parameters, including needle electrode configuration, needle diameter, grid size, and gap between electrodes. The breakdown voltage and highest velocity corresponding to the breakdown voltage increase with an increase in the needle tip-to-mesh gap. After parametric optimization, a maximum velocity of 2.55 m/s and a flow rate of 2868 L/min are achieved.
[DOI: 10.1115/1.4041391]

Keywords: ionic wind pump, volumetric flow rate, numerical simulation

1 Introduction

When a high electric potential difference is applied between two electrodes with different curvature radii, the air molecules around the discharge region are ionized and moved thereafter to the collector electrode using Coulomb force. The moving ions will collide with neutral air molecules and transfer momentum to the surrounding molecules. Thereafter, an airflow, which is called ionic wind, is produced between the corona and collector electrodes. Meanwhile, wind-driven devices that operate based on the ionic wind principle are called electrostatic air accelerators, ionic wind generators, or ionic wind pumps. The devices have attracted considerable attention for their various applications, such as flow control [1,2], heat transfer [3,4] and enhanced combustion [5,6], and propulsion by electrohydrodynamic (EHD) thrusters [7,8] due to of their low energy consumption, compact structures, flexible designs, and lack of moving parts [9,10].

Many researchers have focused on increasing ionic wind velocity and flow rate, which are the key challenges for ionic wind pump. Different electrode configurations, many of which are experimental in nature, have been developed for ionic wind pump. Rickard et al. [11] investigated an ionic wind generator with a pin-to-ring electrode system and attached a converging nozzle to the downstream of the collector electrode; however, velocity was only slightly increased. A wire–non-parallel plate EHD gas pump was investigated by designing a converging electrode configuration instead of attaching a nozzle to the exit of the pump due to the nonparallel plate electrode; a maximum velocity of 1.9 m/s and volumetric flow rate of 44 L/min were observed [12,13]. The flow characteristics of a wire-to-rod EHD gas pump were experimentally investigated and determined that a maximum gas flow rate of 40.1 L/min was generated for a pipe with a diameter of 20 mm, grounding rod electrode diameter of 3.1 mm, and corona wire-to-rod electrode gap of 12.6 mm [14]. Moreover, several researchers attempted to enhance the velocity by staging several ionic wind generators in serials. A serial-staged EHD gas pump was developed under a negative corona discharge in air, in which the flow velocity was dependent on the number of serial stages and pressure loss [15]. Their study indicated a maximum average flow velocity of 7.39 m/s and flow rate of 140 L/min. In their later research [16], Qiu et al. observed a maximum velocity of 16.1 m/s and volumetric flow of 303.5 L/min in a 25-stage gas pump. Lee et al. [17] aimed to further increase flow rate using a novel ionic wind generator, in which many single ionic wind generators were tightly integrated parallel to printed circuit boards. This integrated system achieved a wind speed of 2.2 m/s and flow rate of 800 L/min. Huang et al. [18] designed an EHD-integrated cooling system, in which needle-arrayed electrodes generated ionic wind to cool down a plate fin heat sink. Experiments were performed in a 0.5 m × 0.5 m × 0.65 m (L × W × H) chamber and achieved a heat transfer enhancement ratio of approximately 3–5 under a moderate test condition with preferable normalized electrode height. However, the needle electrodes were simply arranged in arrays; hence, the system was not optimized. In spite of the effort exerted by the aforementioned researchers, a few limitations still exist. First, many of the investigated devices had small cross-sectional areas or limited outlet velocities. Therefore, their volumetric flow rates cannot meet the demands of commercial applications [16,19]. Moreover, the parametric configurations have yet to be investigated in detail, particularly for large cross-sectional ionic wind pump.

Compared with experiments, numerical simulations can provide a substantially detailed analysis of the electrical and flow characteristics of ionic wind pump at a significantly low cost. Various two-dimensional (2D) numerical techniques have been used to

[1]Corresponding author.

Contributed by the Fluids Engineering Division of ASME for publication in the Journal of Fluids Engineering. Manuscript received March 9, 2018; final manuscript received August 29, 2018; published online October 5, 2018. Assoc. Editor: Shizhi Qian.

predict the EHD flow pattern [20]. A numerical modeling was created for both ion-drag pumps and induction EHD pumps using the commercially available computational fluid dynamics software package FIDAP [21]. The simulation results showed that the efficiency of EHD pumps exhibited a strong dependence on bulk fluid velocity. Zhao and Adamiak [22] aimed to obtain the characteristics in the pin-plate and pin-grid configurations by solving the electric field and space charge densities using a numerical algorithm, as well as solving the airflow using the commercial code FLUENT. Experimental data obtained with a hot-wire anemometer were used to validate the simulation results. A computational fluid dynamics analysis of an ionic wind generator with a cantilever structure was conducted for forced convection cooling [23]. The electrostatic, charge transport, fluid dynamic, and heat transfer domain equations were solved in COMSOL MULTIPHYSICS (formerly FEMLAB). The three-dimensional (3D) cantilever structure was approximated using a 2D axial symmetry model. A few assumptions, which included rounded cantilever tips and cross-sectional corners, nonexistent electric field, and fluid dynamics caused by the rest of the cantilever structure, were used. In their later research, Jewell-Larsen et al. [24] developed a numerical model to predict particle motion and address the problem of dust particle accumulation in the EHD systems by adding particle collection behavior to their previous model. The numerical model was verified by operating the ionic wind generator in a dust testing system and measuring the thickness and size of the dust collected. Some researchers also use simulation methods to investigate on dielectric barrier discharge, which is an EHD pump with alternating current (AC) supply [25]. A computational method was developed [26] to couple the EHD body forces induced by dielectric barrier discharges actuation with unsteady Reynolds-averaged Navier–Stokes model or large eddy simulation for incompressible flows. The EHD body force model is based on solving the electrostatic equations for electric potential and net charge density. The boundary condition for net charge density on the dielectric surface is obtained from a space–time lumped-element circuit model or an empirical model. The aforementioned 2D approaches adopt numerous assumptions, thereby possibly causing low accuracy. A 3D numerical model was established with wire-duct configuration in FLUENT by adding user-defined functions [27]. This researcher also used the simulations to discuss a range of monodisperse particle diameters, dilute particle concentration, and negligible particle space charge. The influence of the EHD flow on particle collection was also investigated. A small duct or a typical unit has been applied as the numerical model in the previous numerical studies. To the best of our knowledge, the flow characteristics of large cross-sectional ionic wind pump have yet to be simulated using numerical analyses.

This study designs a large cross-sectional ionic wind pump with multi-needle-to-mesh electrode system. A 3D model of the pump is established and validated by experimental measurements. Thereafter, a simulation method is adopted to obtain the flow characteristics of the ionic wind pump and to optimize the space between the needle electrodes. Grid size, needle tip-to-mesh gap, and diameter of the needle electrode are optimized through experiments. Finally, the ionic wind pump with the optimized parameters is tested experimentally.

2 Experimental Rig Design

The experiment setup is shown in Fig. 1(*a*). The main components of the experimental system include a high-voltage power supply, ionic wind pump test unit, and rotating anemometer. The high-voltage direct current (DC) power supply (TRC2020N20-300, 50 kV, 300 W) is used to apply a high electric potential difference between two electrode boards. The corona electrode board is charged with a high negative voltage, and the collector electrode board is grounded. The voltage and total current are obtained from the voltmeter of the power supply and the maximum measured error is 0.1%. The wind speed is measured using a rotating anemometer (Victor 816B), and the uncertainty is 0.32%. The anemometer is placed in six different locations at the exit to obtain the average outlet velocity. The flow rate of the ionic wind pump is calculated by multiplying the average velocity with the cross-sectional area of the board. All results, including the applied voltage, time-averaged current, and velocity, are tested five times to obtain the average values.

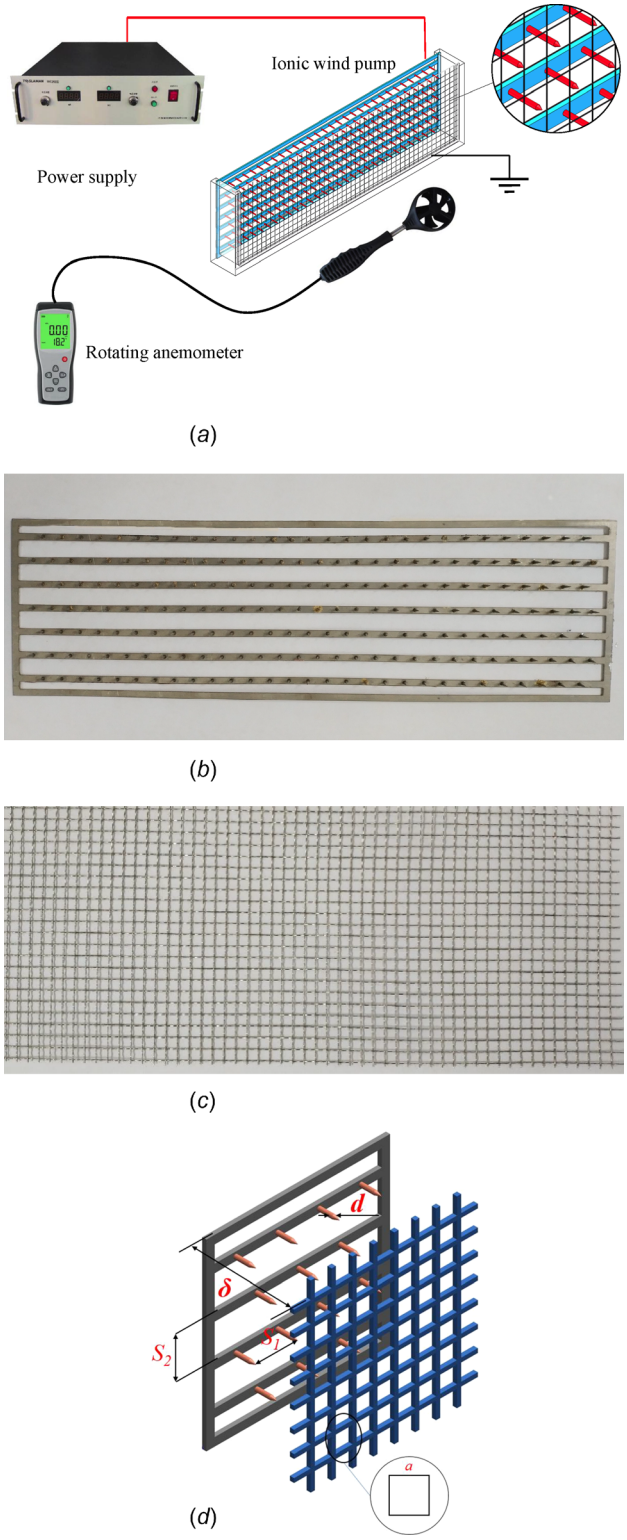

Fig. 1 Experimental setup and ionic wind pump: (*a*) diagram of the experimental setup, (*b*) the corona electrode board, (*c*) the collector electrode board, and (*d*) diagram of the needle configuration, needle diameter, needle tip-to-mesh gap and grid unit

An ionic wind pump with a multi-needle-to-mesh electrode configuration is developed (see Fig. 1(*b*)). The pump comprises a corona electrode board and a separate collector electrode board (see Figs. 1(*c*) and 1(*d*), respectively). The corona electrode board consists of several metal strips with small holes. The diameters of the holes are slightly smaller than those of the needle electrodes, thereby enabling the needles to be directly embedded into these holes. Accordingly, this system can effectively reduce contact resistance and enhance the electrical conductivity of the needle electrodes. The needles are made of tungsten, thereby making the device stable and durable. A high negative voltage is applied to the needle electrodes, and the sharp tips of the needle electrodes face the collector electrode board. The iron wire mesh is used as the collector electrode board. The size of the cross section of the boards is 250 mm × 75 mm (L × W). A glass shell with the same cross-sectional area as the electrode boards is designed to assemble the electrode boards. The two electrode boards can be directly assembled into the shell, and the distance between the two boards can be adjusted with a gap of 3 mm. The test unit, including the two electrode boards and the glass shell, is tested in the measuring system (see Fig. 1(*a*)) to obtain the experimental results.

The geometric parameters of the wind pump are illustrated in Figs. 1(*e*) and 1(*f*). The needle electrode configuration for the transverse space between the two adjacent needles is defined as S_1, while the longitudinal space between the two metal strips is defined as S_2. The diameter of the needle electrode (d), grid size of the mesh, (a) and gap between the needle tip and mesh (δ) are measured. A default model is established as the starting point of the present study. Table 1 shows the parameters of the default model. A few parameters are discussed and changed, and other parameters are maintained as default values.

3 Physical and Mathematical Models

3.1 Physical Model. The default model is established to simulate the electrical and flow characteristics of the ionic wind pump. The physical model comprises needle and collector electrode boards (see Fig. 2(*a*)). A computational domain with a side length of 40 mm is selected to reduce computational time and cost. Air is introduced at the inlet and flows through the area between the two electrode boards. Thereafter, the airflow reaches and flows through the mesh electrode.

3.2 Governing Equations and Boundary Conditions. The electrical potential in the inter-electrode space of the ionic wind pump is described by Poisson's equation for electrostatics as follows:

$$\nabla^2 V = -\frac{q}{\varepsilon_0} \tag{1}$$

Where q is the space charge density, which is the measure of the amount of electric charge per unit volume. The dielectric permittivity of free space ε_0 is chosen as 8.85×10^{-12} F/m. The electric field is represented by **E**, where

$$\mathbf{E} = -\nabla V \tag{2}$$

The conservation of current density equation is as follows:

$$\nabla \mathbf{J} = 0 \tag{3}$$

Table 1 Parameters of the default model

Transverse space (S_1)/mm	Longitudinal space (S_2)/mm	Grid size (a)/mm	Needle tip-to-mesh gap (δ)/mm	Needle electrode diameter (d)/mm
10	10	4	16	0.85

where **J** is the current density. Electric current is a combination of three effects: conduction, convection, and diffusion [23]. Therefore, current density **J** can be calculated from the following equation:

$$\mathbf{J} = \mu_E \mathbf{E} q + \mathbf{U} q - D \nabla q \tag{4}$$

where μ_E is the air ion's mobility in an electric field and is chosen as 2.7×10^{-4}. D is the diffusivity coefficient of ions. Considering that the velocity of charged particles is far larger than the air flow velocity and the diffusivity coefficient of ions is quite small [28], the current density is simplified as

$$\mathbf{J} = \mu_E \mathbf{E} q \tag{5}$$

The continuum equation is as follows:

$$\nabla \cdot (\rho \mathbf{U}) = 0 \tag{6}$$

The bulk body force couples the electrostatic equations with the NS equation that governs the flow of the neutral gas medium as follows:

$$\mathbf{U} \cdot \nabla(\mathbf{U}) = -\frac{1}{\rho}\nabla p + \nu \nabla^2 \mathbf{U} + \frac{\mathbf{F}_e}{\rho} \tag{7}$$

where $\mathbf{F}_e$ can be expressed as follows:

$$\mathbf{F}_e = q\mathbf{E} \tag{8}$$

The boundary conditions of the electrostatic, space charge, and velocity fields are provided to solve the preceding equations, as shown in Table 2. A constant DC voltage is applied to the needle electrode board, and the collector electrode board is grounded. The other surfaces, including the inlet and outlet, are assumed to be zero charge. For the charge transport, the gap between the corona and collector electrodes can be divided into two regions, namely, the ionization and drift zones. In the ionization zone, the air is positively and negatively ionized. In the drift zone, the electric field produces a single polarity of negative ions. The effect of the bipolar region of the ionization zone is ignored because the majority of the ionization region volume has a net space charge. After neglecting the ionization zone, the effect of ionization zone is assumed as a boundary condition (q_0) of the interface crossing ionization zone and drift area. The determination of the value of q_0 is based on the Kaptsov [29] hypothesis and Peek's formula [30]. It is assumed in the hypothesis that the interface electric field will preserve its corona onset value after the corona is initiated. The corona onset value can be obtained with Peek's formula [30] as shown in the following equation:

$$E_e = E_0(1 + 2.62 \times 10^{-2}/\sqrt{R_e}) \tag{9}$$

where R_e is the needle electrode's radius and $E_0 = 3.31 \times 10^6$ V/m is the breakdown electric strength of air.

The solved interface electric field can match with Peek's formula [29] with appropriate assumed q_0. Therefore, the q_0 can be gained using the iteration method. The supposed value of q_0 is used to solve the Poisson's equation and the current density conservation equations to obtain the value of E_e. Thereafter, the solved value of E_e is compared with the result from Peek's formula. The initial assumption for q_0 is eventually updated and iterated continuously until the relative deviation of E_e between two successive iterations is below 3%. The solution is conserved to be converged and the final fields of charge density are obtained. A zero diffusive charge flux condition is imposed on the surface for all the other boundaries. As is shown in Table 2, pressure conditions are assigned to the inlet and outlet surfaces for fluid dynamics, and no-slip boundary conditions are applied to the surfaces of the electrodes and other walls.

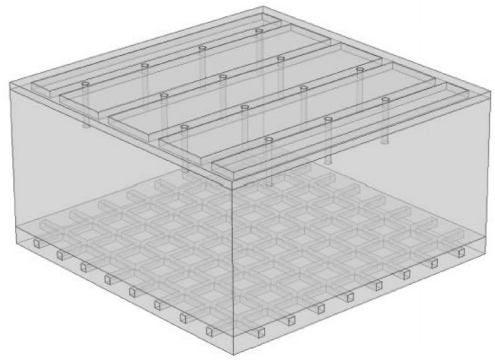

(*a*)

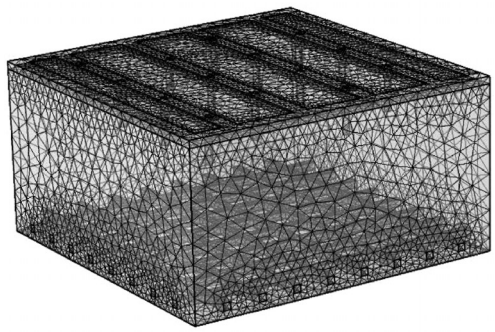

(*b*)

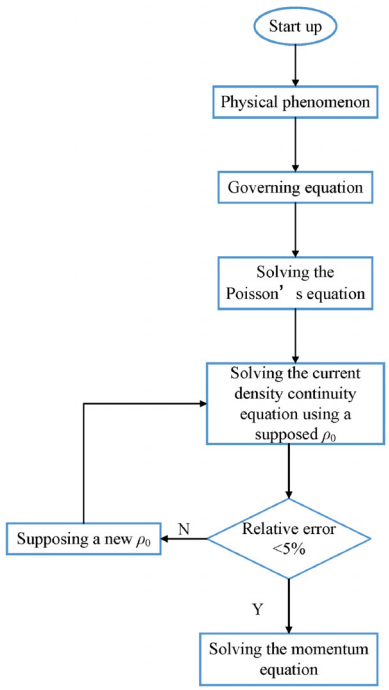

(*c*)

Fig. 2 Physical model: (*a*) physical model, (*b*) mesh of the calculation model, and (*c*) simulation process

3.3 Solution Methods. The commercial software COMSOL MULTIPHYSICS is used to generate regular tetrahedral mesh sets for the simulation process. The mesh around the needle and collector electrodes has been densified to improve the calculation accuracy.

Table 2 Boundary conditions of the physical model

Surface	Electrostatic field	Space charge field	Velocity field
Corona electrode	$V = V_0$	$q = q_0$	$U = 0$
Collector electrode	$V = 0$	$\frac{\partial q}{\partial n} = 0$	$U = 0$
Inlet	$\frac{\partial V}{\partial n} = 0$	$\frac{\partial q}{\partial n} = 0$	$p = p_{env}$
Outlet	$\frac{\partial V}{\partial n} = 0$	$\frac{\partial q}{\partial n} = 0$	$p = p_{env}$
Others	$\frac{\partial V}{\partial n} = 0$	$\frac{\partial q}{\partial n} = 0$	$U = 0$

Five mesh sets (i.e., 85,015, 165,234, 335,100, 632,210, and 1,485,695) are generated in the mesh independence analysis. The evaluation index is the average outlet velocity, which increases by only 0.78% between the fourth and fifth mesh sets when the mesh number increases by 135%. Therefore, the fourth mesh set (i.e., 1,485,695) is selected by a compromise between accuracy and computational consumption. The mesh of the physical model is shown in Fig. 2(*b*).

The simulation is also operated in COMSOL MULTIPHYSICS (see Fig. 2(*c*)). First, Poisson's equation is solved in the electrostatic module. For space charge density, a coefficient partial differential equation module is adopted to solve the current density continuity equation. The value of q_0 on the surface of the needle electrode is iterated until the needle electrode electric field is sufficiently close to the Peek's value. This method provides an indirect boundary condition for space charge density. Finally, the flow characteristics are simulated in the laminar flow module.

3.4 Numerical Model Validation. The default model is selected to verify the simulation method. The simulation values of the average outlet velocity are compared with the experimental results tested in the experimental test rig with the applied voltages ranging from 10 kV to 15 kV. The results of the simulation validation are presented in Fig. 3. The maximum relative deviation of the average outlet velocity is 8.8% under an applied voltage of 15 kV. Therefore, the simulation method is reliable.

4 Numerical Results and Discussion

4.1 Flow Characteristics of the Ionic Wind Pump. The default model is calculated to obtain the electrical and flow characteristics of the ionic wind pump. The electrical and flow field distribution of the default model under an applied voltage of 15 kV is illustrated in Fig. 4. The electrical potential of the needle electrodes and metal strips is higher than that of the mesh electrodes (see Fig. 4(*a*)). Hence, Coulomb force is produced due to the potential difference and pushes the air to flow toward the outlet. The 3D fluid field distribution is shown in Fig. 4(*b*). Air is introduced through the gaps between two adjacent metal strips and continues to flow toward the mesh electrode. Wind speed is locally intensified around the needle electrode because air has been accelerated by the Coulomb force around the needle electrodes. After flowing through the mesh electrode, airflow becomes increasingly separated and accelerated in several local areas near the outlet. A slice in the y–z plate ($x = 20$ mm) of the fluid field is shown in Fig. 4(*c*). The highest velocity appears near the outlet due to the locally accelerating effect of the mesh electrode.

4.2 Numerical Optimization of the Needle Electrode Configuration. The simulation method is adopted based on the flow characteristics of the ionic wind pump to optimize the arrangement of the needle electrodes and obtain a high outlet velocity. If experiments are adopted to optimize the needle electrode configuration, then electrode boards with different needle

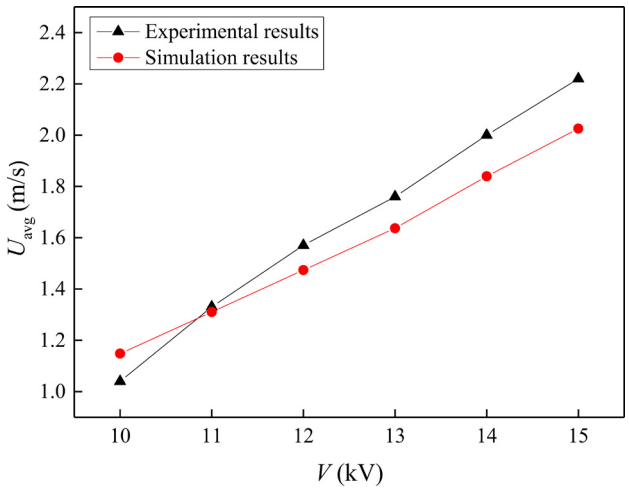

Fig. 3 Verification of the simulation method

electrode configurations need to be built. Nearly 100–200 needles need to be installed on each board, which is a time-consuming process. However, the transverse and longitudinal spaces of the needle electrodes can be easily adjusted when building the simulation models.

Two models are established to optimize the design of the needle electrodes. The longitudinal spaces S_2 remain to be 10 mm and 8 mm for models A and B, respectively. Here, the effect of longitudinal space is not mainly considered. With decreasing the longitudinal space, the number of needle strips increases, leading to the significant increase of needle numbers. This will increase the power consuming and manufacturing cost, which is not suitable for the practical utilization of the pump. So, the main parameter discussed in this paper is the transverse space between needles. The average outlet velocity of each model is measured when the transverse space ranges from 4 mm to 16 mm (the gap is 2 mm). The average outlet velocity is a function of the transverse space (see Fig. 5). A considerable amount of air is ionized near the needle electrodes to enhance wind speed in a small transverse space, in which many needles are arranged on one metal strip. However, the interference between the adjacent needle electrodes becomes increasingly noticeable. As indicated in Refs. [17] and [18], this interference negatively affects velocity. Therefore, the two opposing effects compete to cause the velocity of both models to first increase and then decrease with increased S_1. The maximum velocity is obtained with the transverse space of 8 mm. In addition, the velocity of model A is higher than that of model B with the same transverse space as S_1. Therefore, the reference transverse and longitudinal spaces are selected as 8 mm and 10 mm, respectively. Accordingly, an average outlet velocity of 2.42 m/s is obtained as reference for further optimization.

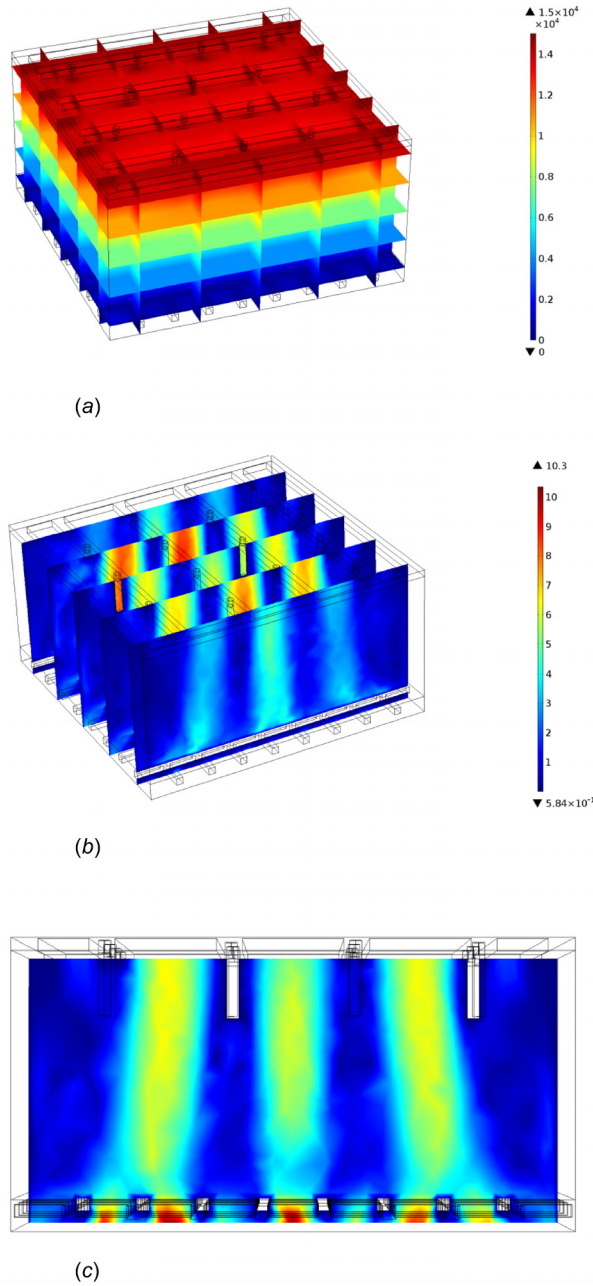

Fig. 4 Electrical and flow field distribution (default model): (*a*) 3D electrical field distribution, (*b*) 3D flow field distribution, and (*c*) slice of the flow field distribution (*y–z* plate, $x = 20$ mm)

5 Experimental Characterization of Ionic Wind Pump

Experiments are adopted based on the optimum needle electrode configuration to analyze the effect of needle electrode diameter, mesh grid size (collector electrode), and needle tip-to-mesh gap on the flow characteristics of ionic wind pump. The adjustment of the aforementioned parameters can be easily realized in the experiments. The tip-to-mesh gap may significantly affect the breakdown voltage, which determines the maximum velocity. However, the breakdown value cannot be predicted in the current simulation method. Therefore, experimental measurements are indispensable when analyzing the tip-to-mesh gaps. Therefore, experimental methods are adopted for analysis and optimization.

5.1 Effect of the Needle Electrode Diameter. Needle diameters of 0.85 mm and 1 mm are investigated. The average outlet velocity at the two needle electrode diameters is shown in Fig. 6. Accordingly, the thinner the needles, the higher the velocity that can be obtained. With thin needles, the curvature radius difference of the needle and collector electrodes becomes substantially large, thereby causing more non-uniform electric field, resulting in the ionization of numerous air molecules around the needle electrodes. Therefore, space discharge density increases, thereby leading to the increase of the average outlet velocity. The diameter of the needle electrode is set at 0.85 mm, which is the smallest needle diameter that can be adopted in the experiments due to the limitation of our manufacturing process for drilling holes in the metal strips of the corona electrode board.

5.2 Effect of the Mesh Grid Size. The fundamental role of the geometry of the collector electrode is investigated. The effects of grid size on the average outlet velocity and power consumption

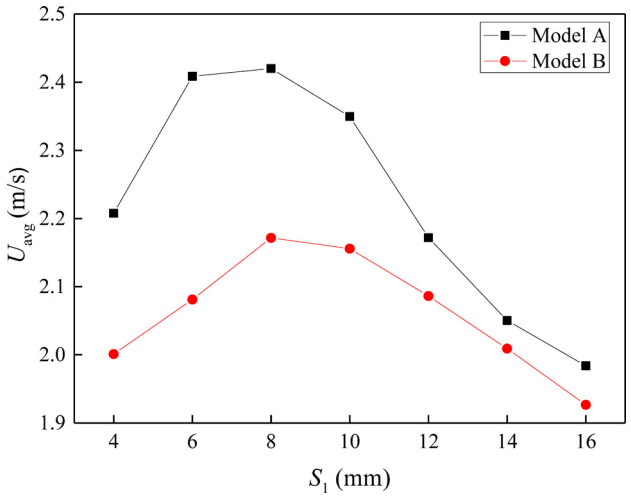

Fig. 5 Average outlet velocity as a function of the transverse space

are illustrated in Fig. 7. Velocity increases with an increase in the applied voltage (see Fig. 7(*a*). At the same applied voltage, an optimum grid size is obtained and associated with the highest velocity. Two competing factors influence wind speed with an increase in grid size. On the one hand, the available collector area for the mesh electrode becomes smaller as the grid becomes larger, thereby possibly reducing the outlet velocity. On the other hand, flow resistance rapidly decreases as the mesh electrode becomes less dense, thereby resulting in an increase in wind speed. The optimum value to obtain the maximum velocity is chosen as 4 mm, which is due to the combined effects of available area of collector electrode and the flow resistance.

The power consumption of ionic wind pump is also influenced by the electrical and flow characteristics. The power consumption of the pump at different grid sizes is illustrated in Fig. 7(*b*). Power is the highest at the grid size of 2 mm, which may be attributed to the high flow resistance accompanied by a substantial energy loss. The power consumption is close for $a = 6$ mm and $a = 8$ mm. By comprehensively considering the velocity and power consumption, the optimum grid size of 4 mm is selected.

5.3 Effect of the Needle Tip-to-Mesh Gap. The gap between the needle tip and mesh is another geometric parameter that significantly affects the performance of ionic wind pump. The

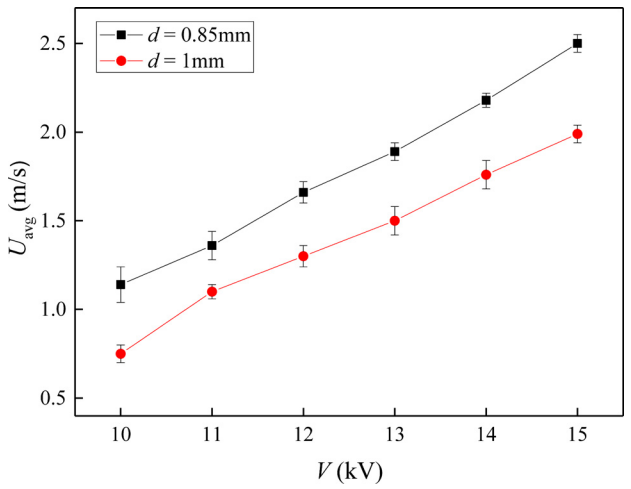

Fig. 6 Average outlet velocity at different diameters of the needle electrode

average outlet velocity at different gaps and applied voltages is presented in Fig. 8. A substantially high voltage is required to achieve the same average outlet velocity with a large gap. This requirement is attributed to a large gap between two electrodes that may result in weak electric field strength accompanied by weak forces and low wind speed. At a fixed gap, the achieved velocity increases with increasing the applied voltage, and the maximum velocity can be obtained at the breakdown voltage. The breakdown voltage increases with the increased tip-to-mesh gap because a considerably high voltage is required to reach the energy limit for breakdown with a large gap. In addition, the achieved maximum velocity increases slightly with an increase in the gap. Evidently, maximum velocity exhibits small incremental increases. When the gap ranges from 10 mm to 22 mm, the maximum velocity increases by only 27%, whereas the applied maximum voltage increases by 130%. This result means that considerable energy consumption is necessary at a large gap to achieve a higher velocity.

To obtain high wind speed with low energy consumption, the effect of the needle tip-to-mesh gap on the electric-to-kinetic energy conversion efficiency [31] is investigated. The efficiency is defined as follows:

$$\eta = \frac{\frac{1}{2}\dot{m}U_{avg}^2}{P} = \frac{\frac{1}{2}\rho A U_{avg}^3}{P} \tag{10}$$

Table 3 shows the breakdown voltage, average outlet velocity, power consumption, and efficiency at different needle tip-to-mesh

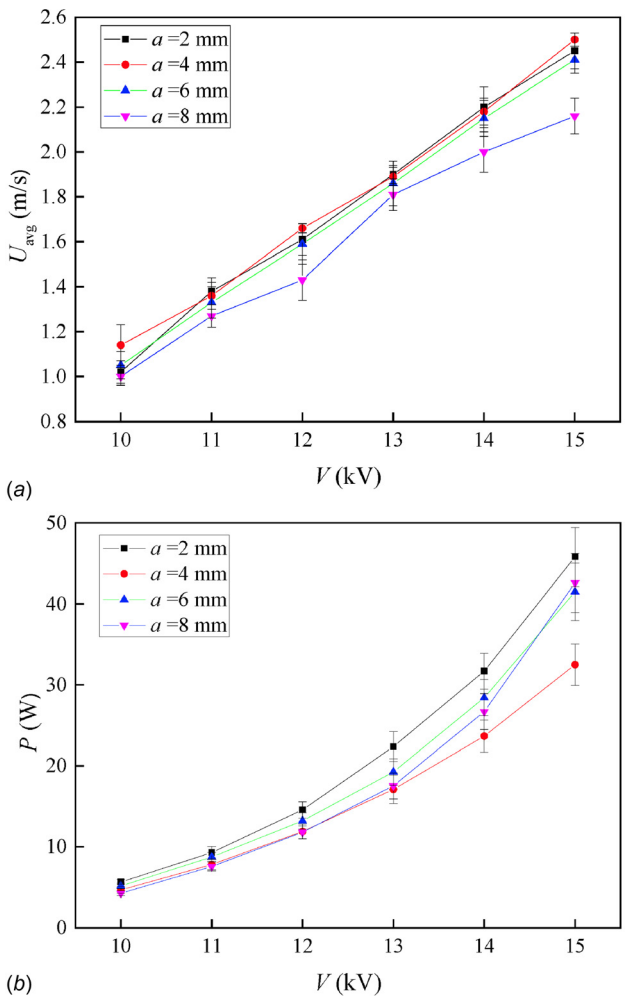

Fig. 7 Effects of different grid sizes: (*a*) the average outlet velocity at different grid sizes and (*b*) the power consumption at different grid sizes

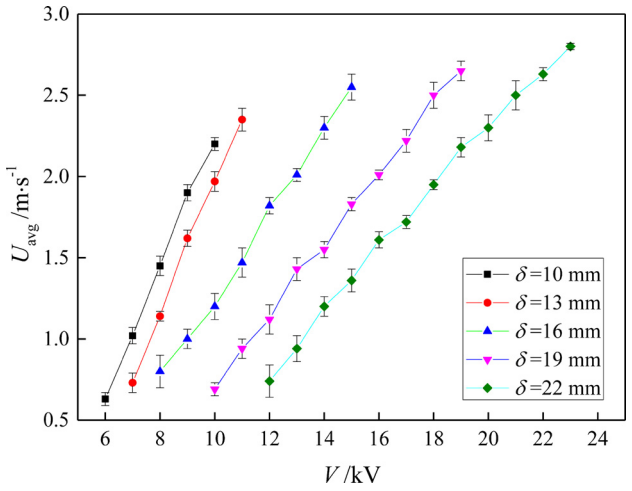

Fig. 8 Average outlet velocity at different needle tip-to-mesh gaps

Table 3 Breakdown voltage, average outlet velocity, power consumption, and efficiency at different needle tip-to-mesh gaps

Needle tip-to-mesh gap (δ)/mm	Breakdown voltage (V)/kV	Average outlet velocity (U_{avg})/m·s^{-1}	Power consumption (P)/W	Efficiency (η)
10	10.0	2.2	27.31	0.473%
13	12.0	2.35	26.71	0.589%
16	15.2	2.55	32.49	0.618%
19	19.5	2.65	39.38	0.572%
22	23.0	2.8	50.16	0.530%

gaps. An increase in the gap results in the initial increase and eventual decrease in efficiency. The efficiency is highest when $\delta = 16$ mm. The required voltage substantially increases with maximum speed. Therefore, the efficiency decreases when δ increases from 16 mm to 22 mm. When $\delta = 16$ mm, the maximum velocity is 2.55 m/s, which is acceptable for a large cross-sectional ionic wind pump. In addition, the efficiency is highest at this gap. Therefore, 16 mm is selected as the best value of δ.

5.4 Test Performance of the Optimized Ionic Wind Pump. A preferred parameter combination ($S_1 = 8$ mm, $S_2 = 10$ mm, $d = 0.85$ mm, $a = 4$ mm, and $\delta = 16$ mm) is selected based on the parametric optimization by simulation and experimental methods. The performance of the ionic wind pump is tested experimentally using the aforementioned structural parameters. Table 4 shows the results. The average outlet velocity is 2.55 m/s when the voltage is 15 kV. The speed is improved compared with the integrated ionic wind generator developed by Lee et al. [17]. The flow rate per unit power is 1.47 L/(s W), which approximates that of conventional fans ranging from 1 L/(s W) to 4 L/(s W) [32]. In addition, ionic wind pump are advantageous because they have compact structures, low noise levels, and no moving parts. Therefore, ionic wind pump can be applied for air supply and heat transfer enhancement.

Table 4 Performance of the ionic wind pump

Voltage (V)/kV	Average outlet velocity (U_{avg})/m·s^{-1}	Flow rate (Q)/L·min^{-1}	Power consumption (P)/W	Flow rate per unit power/L·s^{-1}·W^{-1}
15.0	2.55	2868	32.49	1.47

6 Conclusion

An ionic wind pump is developed, and numerical and experimental analyses are performed to evaluate its flow characteristics and to optimize its parametric configurations. The numerical method is validated by the experimental results. The optimum values of the transverse and longitudinal spaces of the needle electrodes have to be met to obtain a high outlet velocity because of the comprehensive effect of interference between the needles and increase in needle density. The optimum values are 8 mm and 10 mm for S_1 and S_2, respectively. Accordingly, the thinner the needles, the higher the average outlet velocity. The optimum value of a is set at 4 mm due to the combined effect of increasing the grid unit length, and the power is also the lowest. The larger the tip-to-mesh gap, the higher the maximum speed that can be obtained and the higher the required voltage. A tip-to-mesh gap of 16 mm is selected to obtain the highest efficiency value. After optimization, the average outlet velocity is 2.55 m/s, and the volumetric flow rate is 2868 L/min. The flow rate per unit power is 1.47 L/(s W), which approximates that of conventional fans.

Funding Data

- The National Natural Science Foundation of China (No. 51576155).
- The Foundation for Innovative Research Groups of the National Natural Science Foundation of China (Grant No. 51721004).

Nomenclature

A = cross-sectional area, m^2
A = length of the grid unit, mm
d = diameter of the needle electrode, mm
D = diffusivity coefficient of ions, m$^2 \cdot$ s^{-1}
E = electric field intensity, V $\cdot$ m^{-1}
F = electric force, N
I = current, A
J = current density, A $\cdot$ m^{-1}
m = mass flow rate, kg $\cdot$ s^{-1}
n = normal direction, m
p = pressure, Pa
P = electric power, W
q = space charge density, C $\cdot$ m^{-3}
Q = flow rate, L $\cdot$ min^{-1}
R = radius of the needle electrode, mm
S = space between needles or metal strips, mm
δ = tip-to-mesh gap, mm
U = velocity, m $\cdot$ s^{-1}
V = voltage, V

Greek Symbols

ε = dielectric constant, F $\cdot$ m^{-1}
η = electric-to-kinetic energy conversion efficiency, %
μ = ionic mobility, m$^2 \cdot$ V$^{-1} \cdot$ s^{-1}
ν = kinematic viscosity, m$^2 \cdot$ s^{-1}
ρ = density, kg $\cdot$ m^{-1}

Subscripts

avg = value of the average
E = value under the electric field
env = environment
max = value of the maximum
0 = value of initial
1 = transverse value
2 = longitudinal value

References

[1] Zhao, P., Portugal, S., and Roy, S., 2015, "Efficient Needle Plasma Actuators for Flow Control and Surface Cooling," Appl. Phys. Lett., **42**(4), pp. 031176–032004.

[2] Lakeh, R. B., and Molki, M., 2010, "Patterns of Airflow in Circular Tubes Caused by a Corona Jet With Concentric and Eccentric Wire Electrodes," ASME J. Fluids Eng., **132**(8), p. 081201.
[3] D. H. S., Baek, S. H., and Han, S. K., 2016, "Development of Heat Sink With Ionic Wind for LED Cooling," Int. J. Heat Mass Transfer., **93**, pp. 516–528.
[4] Wang, S., Zhang, J., Kong, L., Qu, Z., and Tao, W., 2017, "An Numerical Investigation on the Cooling Capacity of Needle-Ring Type Electrostatic Fluid Accelerators for round Plate With Uniform and Non-Uniform Heat Flux," Int. J. Heat Mass Transfer., **113**, pp. 1–5.
[5] Jacobs, S. V., and Xu, K. G., 2016, "Examination of Ionic Wind and Cathode Sheath Effects in a E-Field Premixed Flame With Ion Density Measurements," Phys. Plasmas., **23**(4), p. 156.
[6] Park, D. G., and Chung, S. H., Cha, M. S., 2016, "Bidirectional Ionic Wind in Nonpremixed Counterflow Flames With DC Electric Fields," Combust. Flame., **168**, pp. 138–146.
[7] Hasnain, S. M., Bakshi, A., and Selvaganapathy, P. R., C. Y. C., 2011, "On the Modeling and Simulation of Ion Drag Electrohydrodynamic Micropumps," ASME J. Fluids Eng., **133**(5), pp. 2444–2453.
[8] Monrolin, N., Plouraboué, F., and Praud, O., 2017, "Electrohydrodynamic Thrust for in-Atmosphere Propulsion," AIAA J., **55**(12), pp.1–10.
[9] Fylladitakis, E. D., Theodoridis, M. P., and Moronis, A. X., 2014, "Review on the History, Research, and Applications of Electrohydrodynamics," IEEE Trans. Plasma Sci., **42**(2), pp. 358–375.
[10] Johnson, M. J., and Go, D. B., 2017, "Recent Advances in Electrohydrodynamic Pumps Operated by Ionic Winds: A Review," Plasma Sources Sci. Technol., **26**(10), pp. 1–27.
[11] Rickard, M., Dunn-rankin, D., Weinberg, F., and Carleton, F., 2005, "Characterization of Ionic Wind Velocity," J. Electrostatics., **63**(6–10), pp. 711–716.
[12] Tsubone, H., Ueno, J., Komeili, B., Minami, S., Harvel, G. D., Urashima, K., Ching, C. Y., and Chang, J. S., 2008, "Flow Characteristics of dc Wire-Non-Parallel Plate Electrohydrodynamic Gas Pumps," J. Electrostatics., **66**(1–2), pp. 115–121.
[13] Chang, J. S., Tsubone, H., Chun, Y. N., Berezin, A. A., and Urashima, K., 2009, "Mechanism of Electrohydrodynamically Induced Flow in a Wire-Non-Parallel Plate Electrode Type Gas Pump," J. Electrostatics., **67**(2–3), pp. 335–339.
[14] Komeili, B., Chang, J. S., Harvel, G. D., Ching, C. Y., and Brocilo, D., 2008, "Flow Characteristics of Wire-Rod Type Electrohydrodynamic Gas Pump Under Negative Corona Operations," J. Electrostatics., **66**(5–6), pp. 342–353.
[15] Qiu, W., Xia, L., Tan, X., and Yang, L., 2010, "The Velocity Characteristics of a Serial-Staged EHD Gas Pump in Air," IEEE Trans. Plasma Sci., **38**(10), pp. 2848–2853.
[16] Qiu, W., Xia, L. Z., Yang, L. J., Zhang, Q. G., Lei, X., and Lin, C., 2011, "Experimental Study on the Velocity and Efficiency Characteristics of a Serial Staged Needle Array-Mesh Type EHD Gas Pump," Plasma Sci. Technol., **13**(6), p. 693.
[17] Lee, S. J., Li, L., Kwon, K., Kim, W., and Kim, D., 2015, "Parallel Integration of Ionic Wind Generators on PCBs for Enhancing Flow Rate," Microsyst. Technol., **21**(7), pp. 1465–1471.
[18] Huang, R. T., Sheu, W. J., and Wang, C. C., 2009, "Heat Transfer Enhancement by Needle-Arrayed Electrodes—An EHD Integrated Cooling System," Energy Convers. Manage., **50**(7), pp. 1789–1796.
[19] Moon, J. D., Hwang, D. H., and Geum, S. T., 2009, "An EHD Gas Pump Utilizing a Ring/Needle Electrode," IEEE Trans. Dielectrics Electr. Insul., **16**(2), pp. 352–358.
[20] Bouazza, M. R., Yanallah, K., Pontiga, F., and Chen, J. H., 2018, "A Simplified Formulation of Wire-Plate Corona Discharge in Air: Application to the Ion Wind Simulation," J. Electrostatics., **92**, pp. 54–65.
[21] Singhal, V., and Garimella, S. V., 2005, "Influence of Bulk Fluid Velocity on the Efficiency of Electrohydrodynamic Pumping," ASME J. Fluids Eng., **127**(3), pp. 484–494.
[22] Zhao, L., and Adamiak, K., 2005, "EHD Flow in Air Produced by Electric Corona Discharge in Pin–Plate Configuration," J. Electrostatics., **63**(3–4), pp. 337–350.
[23] Jewell-larsen, N. E., Hsu, C. P., Krichtafovitch, I. A., and Montgomery, S., 2008, "CFD Analysis of Electrostatic Fluid Accelerators for Forced Convection Cooling," IEEE Trans. Dielectrics Electr. Insul., **15**(6), pp. 1745–1753.
[24] Jewell-larsen, N. E., Karpov, S. V., Ran, H., Savalia, P., and Honer, K. A., 2010, "Investigation of Dust in Electrohydrodynamic (EHD) Systems," 26th Annual IEEE Semiconductor Thermal Measurement and Management Symposium (SEMI-THERM), Santa Clara, CA, Feb. 21–25.
[25] Corke, T. C., Enloe, C. L., and Wilkinson, S. P., 2010, "Dielectric Barrier Discharge Plasma Actuators for Flow Control," Annu. Rev. Fluid Mech., **42**(1), pp. 505–529.
[26] Shan, H., and Lee, Y. T., 2014, "Numerical Modeling of Dielectric Barrier Discharge Plasma Actuation," ASME J. Fluids Eng., **138**(5), p. 051104.
[27] Farnoosh, N., Adamiak, K., and Castle, G. P., 2010, "3-D Numerical Analysis of EHD Turbulent Flow and Mono-Disperse Charged Particle Transport and Collection in a Wire-Plate ESP," J. Electrostatics., **68**(6), pp. 513–522.
[28] Feng, J. Q., 1999, "Application of Galerkin Finite-Element Method With Newton Iterations in Computing Steady-State Solutions of Unipolar Charge Currents in Corona Devices," J. Comput. Phys., **151**(2), pp. 969–989.
[29] Kaptsov, N. A., 1947, *Elektricheskie Yavleniya v Gazakh i Vakuume*, OGIZ, Moscow, Russia.
[30] Peek, F. W., 1920, *Dielectric Phenomena in High Voltage Engineering*, McGraw-Hill Book Company, New York.
[31] Kim, C., Park, D., Noh, K. C., and Hwang, J., 2010, "Velocity and Energy Conversion Efficiency Characteristics of Ionic Wind Generator in a Multistage Configuration," J. Electrostatics., **68**(1), pp. 36–41.
[32] Mazumder, A. H., and Lai, F. C., 2014, "Enhancement in Gas Pumping in a Square Channel With Two-Stage Corona Wind Generator," IEEE Trans. Ind. Appl., **50**(4), pp. 2296–2305.